# HOKKAIDO UNIVERSITY

| | |
|---|---|
| Title | Lift coefficient of bubble sliding inside turbulent boundary layers in an inclinable channel flow |
| Author(s) | Yoon, Dongik; Park, Hyun Jin; Tasaka, Yuji; Murai, Yuichi |
| Citation | Physics of fluids, 34(5), 53301<br>https://doi.org/10.1063/5.0086777 |
| Issue Date | 2022-05-02 |
| Doc URL | http://hdl.handle.net/2115/89152 |
| Rights | This article may be downloaded for personal use only. Any other use requires prior permission of the author and AIP Publishing. This article appeared in Physics of Fluids 34, 053301 (2022) and may be found at https://doi.org/10.1063/5.0086777. |
| Type | article |
| File Information | 5.0086777.pdf |

# Lift coefficient of bubble sliding inside turbulent boundary layers in an inclinable channel flow <span>F</span>

(iD) **Dongik Yoon** (윤동익), (iD) **Hyun Jin Park** (朴 炫珍), (iD) **Yuji Tasaka** (田坂 裕司), **et al.**

**COLLECTIONS**

F   This paper was selected as Featured

View Online     Export Citation     CrossMark

**ARTICLES YOU MAY BE INTERESTED IN**

Swimming of an inertial squirmer array in a Newtonian fluid
Physics of Fluids **34**, 053303 (2022); https://doi.org/10.1063/5.0090898

Numerical analysis of interaction between turbulent structures and transient sheet/cloud cavitation
Physics of Fluids **34**, 047116 (2022); https://doi.org/10.1063/5.0085072

Spectra and structure functions of the temperature and velocity fields in supergravitational thermal turbulence
Physics of Fluids **34**, 055108 (2022); https://doi.org/10.1063/5.0091012

AIP Publishing

Physics of Fluids

# Lift coefficient of bubble sliding inside turbulent boundary layers in an inclinable channel flow Ⓕ

View Online    Export Citation    CrossMark

Dongik Yoon (윤동익),[a] ⓘD Hyun Jin Park (朴 炫珍), ⓘD Yuji Tasaka (田坂 裕司), ⓘD and Yuichi Murai (村井 祐一) ⓘD

### AFFILIATIONS

Laboratory for Flow Control, Graduate School of Engineering, Hokkaido University, N13 W8, Kita-ku, Sapporo 060-8628, Japan

[a]Author to whom correspondence should be addressed: yoon@ring-me.eng.hokudai.ac.jp

### ABSTRACT

The behavior of bubbles traveling in the proximity of a tilted wall is studied experimentally to understand the fundamental sliding motion of bubbles inside turbulent boundary layers along an inclined wall. The qualitative visualization of sliding bubbles confirms the contribution of bubble buoyancy on the sliding motion for negative and positive inclinations of the channel. An opto-acoustic combined measurement technique is adopted to explore the sliding motion. Liquid velocity profiles in the bubbly flow and the distance between the wall and bottom of the bubble are obtained using the ultrasound pulsed Doppler method, while the bubble diameters and velocities are obtained from particle-tracking type image processing. The combined measurements reveal that the velocity of bubbles decreases under the negative slope condition and increases under the positive slope condition due to opposite buoyancy effects. In addition, the distance between the wall and bottom of the bubble increases with an increase in negative inclination. The lift coefficient is derived from the measured variables using a force–balance equation among the buoyancy, lift, and surface tension. Finally, we propose modeling equations for the lift coefficient expressed in terms of the Reynolds, Weber, and Bond numbers, which apply to the bubbles inside boundary layers.

## I. INTRODUCTION

In bubble dynamics, a transverse force has significant effects on bubble behavior. This force is a key to predicting characteristics of bubbly flows in various industrial applications such as heat and mass transfer and drag reduction. For example, it contributes to void fraction distributions in vertical pipes, known as wall-, double-, and core-peak profiles.[1,2] The transverse force can also induce migration of bubbles from near the wall in flat plate turbulent boundary layers, because it is strong enough to surpass the turbulent diffusion that would disperse the bubbles back into the near-wall region.[3] In addition to migration, the balance between the buoyancy and the transverse force determines a critical volumetric air flux required for air layer drag reductions used in the ship industry.[4] This force is generally called the shear-induced lift, and its mechanism was elaborated by Auton;[5] the lift coefficient ($C_L$) is 0.5 for a spherical bubble at high bubble Reynolds numbers ($50 < Re_b < 1000$). However, this result is restricted to perfectly spherical bubbles suspended in linear shear flows.

In other studies of $C_L$, Žun[1] and Bertodano et al.[2] reported that small bubbles have values of $C_L$ ranging from 0.25 to 0.30 in an air-water system. Legendre and Magnaudet[6] proposed a model for $C_L$ of spherical bubbles in a linear shear flow, showing a strong correlation with $Re_b$ and a dimensionless shear rate. Tomiyama et al.[7] reported

that $C_L$ of small bubbles showed dependency on $Re_b$. In contrast, $C_L$ of large bubbles depended on the Bond number ($Bo$), which adopts the maximum horizontal dimension as the characteristic length. Adoua et al.[8] found that the interaction between the shear flow and vorticity around the interface of a deformable bubble can induce a sign reversal in $C_L$ based on a numerical study. In recent studies, Aoyama et al.[9] experimentally investigated the negative $C_L$ of bubbles at low $Re_b$ ($0 < Re_b < 120$) and supported the mechanism[8] for alternation of the sign of $C_L$ in a certain range of the Morton number. Lee and Lee[10] estimated $C_L$ of a rising bubble in a downward linear shear flow at high $Re_b$ ($440 < Re_b < 7200$) and derived a formula for $C_L$ considering the shape oscillation period of the bubble. Hessenkemper et al.[11] recently reported the effect of impurities on the lift and suggested a $C_L$ correlation valid only for bubble sizes less than 6.5 mm, and he also discovered that $C_L$ depends on the degree of contamination with a parabolic trend.[12] Hayashi et al.[13] studied $C_L$ of the deformable bubble in a surface tension-inertial force dominant regime, and Xu et al.[14] investigated $C_L$ at the linear shear flow with a low turbulence intensity level. Although many bubble behavior characteristics have been clarified by the studies above, difficult problems in bubble dynamics remain in practical applications. A representative example is the bubbly drag reduction[15] (BDR) technique used in the ship industry, for which

estimating $C_L$ inside turbulent boundary layers is the primary issue in the control of the near-wall void profile.

Madavan *et al.*[16,17] discovered that up to 80% drag reduction could be achieved with highly concentrated bubbles injected in turbulent boundary layers. A significant number of numerical and experimental studies on BDR have been conducted in the 21st century (e.g., Refs. 18–23) in response to the regulation of the ship exhaust. Ceccio[24] and Murai[25] summarized the basic BDR mechanisms in their review articles. Despite the maximum 80% drag reduction reported in previous studies, studies on the practical application of BDR have shown lower net energy savings of 5%–15% (e.g., Refs. 26–28), and these lower performance values are related to the complicated BDR mechanisms. The BDR efficiency depends on many bubbly flow features below the hull. Among the features, void fraction,[29] deformation,[30] and liquid film thickness[31] that play a key role in the drag reduction can be affected by the lift. Nevertheless, it is difficult to estimate the lift acting on bubbles in the turbulent boundary layer, because most previous studies have dealt with $C_L$ of bubbles in a linear shear flow. This emphasizes the need for fundamental physics studies on $C_L$ in turbulent shear flows to improve BDR.

Meanwhile, BDR studies have employed horizontal systems, even though actual hulls involve significantly tilted surfaces at the bow and stern. In addition, the altitude of a vessel changes continuously with six degrees of freedom due to ocean wave effects. Kawakita and Hamada[32] reported void fraction changes induced by bubble velocity differences on a tilted surface in a ship model experiment. The sliding bubbles over tilted surfaces in a quiescent fluid showed more complex motion than for a flat surface.[33–35] The complex motion is especially enhanced in a liquid base flow. Figure 1 illustrates the situations adopted in the present study. For the slope conditions, the bubble buoyancy ($F_b$) is resolved into two components: one acting parallel to the wall inducing a slip velocity ($F_{b,f}$) and the other acting perpendicular to the wall ($F_{b,w}$). The bubble velocity is decelerated and accelerated by $F_{b,f}$ in down- and up-slope conditions Figs. 1(a) and 1(c), respectively. In contrast, the effect of $F_{b,f}$ is negligible on the velocity in the horizontal system [Fig. 1(b)]. Simultaneously, bubble deformation is also influenced by the contribution of $F_{b,f}$ to the bubble velocity. Then, the distance between the bubble center and the wall varies with the balance among $F_{b,w}$, lift, and other forces. Thus, studies employing a horizontal system are not always valid in the tilted system. There is, therefore, a need to establish a physics-based model of $C_L$ for slope conditions close to real ocean situations. The present study investigates

$C_L$ of bubbles in the turbulent boundary layer adjacent to tilted surfaces.

We constructed an inclinable channel to observe the behavior of bubble wall-sliding in the turbulent boundary layer on a tilted surface. In the experiments, an opto-acoustic combined measurement technique was applied to a bubbly turbulent flow in the inclinable channel. The acoustic measurement combines two types of ultrasound (US) measurements. One is ultrasound pulse echography (UPE) to detect the interface between the gas and liquid phase,[36] and the other is an ultrasound velocity profiler (UVP) to obtain the liquid velocity profile.[37] A type of PTV (particle tracking velocimetry) optical measurement system was also adopted to obtain the diameters and advection velocities of individual bubbles in the boundary layers. The details of the measurement techniques are described in Sec. II. Based on the measurements, we establish a force balance equation to estimate the bubble $C_L$ as a function of $Re_b$, $Bo$, and $We$ (Weber number) with the results discussed in Sec. III. Finally, Sec. IV summarizes the conclusions of the study.

## II. EXPERIMENTAL METHOD

The optical measurement technique entails several challenges in analyzing the bubble behavior. Cameras allow measurement within only a thin, focused sheet, but most bubbles slide in regions out of the sheet. As a result, many unfocused bubbles were observed sliding along the horizontal flat wall, illuminated by the front and rear of the laser sheet, as shown in the left side of Fig. 2(a). In addition, a lens flare can occur caused by the scattering of light, as shown in the right side of the figure. Since these issues complicate the detection of the gas–liquid interface and tracer particles, such optical measurements are not suitable for high $Re_b$ in a turbulent flow.

US measurements can overcome these difficulties. UPE can be constructed based on raw echo signals, which have a periodic interval proportional to the inverse of pulse repetition frequency (i.e., $\Delta t_{UPE} = 1/f_{PRF}$). UPE offers interfacial information with high spatiotemporal resolution, as shown in Fig. 2(b). Our group's studies confirmed the sufficiently high performance of this technique to detect bubble interfaces, which were performed to measure the thickness of a liquid film flowing between moving bubbles and a solid wall in ship model experiments.[31,36] In the present study, UVP was also combined with UPE to simultaneously obtain liquid velocity profiles. The optical measurements were adopted to measure the diameter and velocity of bubbles,
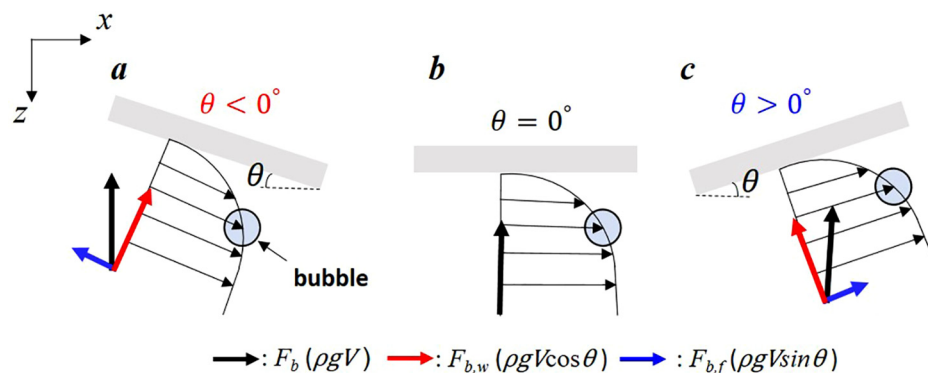


**FIG. 1.** Illustration of slope situations in the present study. (a) Down-slope (a declined condition in the present experiment), (b) horizontal (a flat condition in the present experiment), and (c) up-slope (an inclined condition in the present experiment).
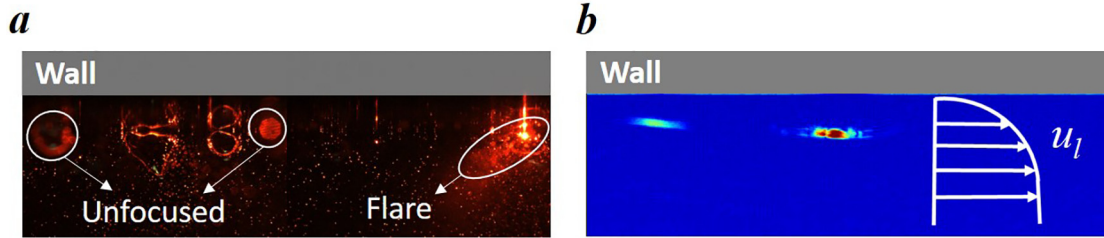
**FIG. 2.** Measurement of sliding bubbles in a side view ($x$–$z$ plane) using (a) optical measurements and (b) US measurements. $u_l$ is the liquid velocity.

because it is difficult to obtain this information with high accuracy using only the US measurements.

## A. Test facility

A schematic diagram of the experimental facility used in the present study is shown in Fig. 3(a). The channel angle ($\theta$) is freely controllable to negative and positive values by a crane. A gas–liquid mixture flowed to the water tank at the end of the channel, and the bubbles were removed in the tank allow only water to enter the pump. A constant liquid flow rate was maintained and monitored by an electromagnetic flowmeter. The test section is a rectangular channel made of transparent acrylic resin and is 2 m in length ($L$), 0.16 m in width, and 0.04 m in height ($H = 2h$), as shown in Fig. 3(b). The air injector, which has five 1-mm-diameter holes, is mounted on the upper wall of the channel at $x/L = 0.05$ from the channel inlet, where the $x$, $y$, and $z$ coordinates represent the streamwise, spanwise, and wall-perpendicular downward directions, respectively. The bubbles were injected at a fixed flow rate controlled by a valve at the air injector, and a flowmeter monitored the air flow rate. There are three angular states of the channel as shown in Fig. 1: (i) the declined condition

(negative angle, $\theta < 0°$), representing the slope surface at the bow of a vessel, (ii) the inclined condition (positive angle, $\theta > 0°$) representing the slope at the stern of a vessel, and (iii) the horizontal ($\theta = 0°$) condition.

A high-speed video camera (CR $600 \times 2$, Optronics) was mounted on top of the channel with an LED panel to measure the diameter and velocity of bubbles. A transducer-holder was installed at the channel bottom and was filled with an ultrasound gel to prevent ultrasound attenuation by the air. Two transducers (TX-4-5-8-40, Met-Flow S.A.) were installed in the holder. One transducer was installed perpendicular to the wall to act as an emitter, and the other was installed with a $10°$ tilt angle ($\gamma$) to act as a receiver, as shown in the blue dashed area of Fig. 3(b). The distance between the centers of the emitter and receiver was 9 mm. The emitter was controlled by a pulser/receiver (JPR-600C, Japan Probe Co., Ltd), and the ultrasound signals reflected by the tracer particles and bubbles were received by the emitter and receiver to a data logger (PicoScope 3405D, Pico Technology). The data logger allowed US measurement without dead time for 5 s with a sampling time ($t_s$) of 40 ns. The position of US measurement coincides with the optical measurement to observe the same bubble over the same measurement time [see the black dashed line in Fig. 3(b)]. The receiver was connected to a
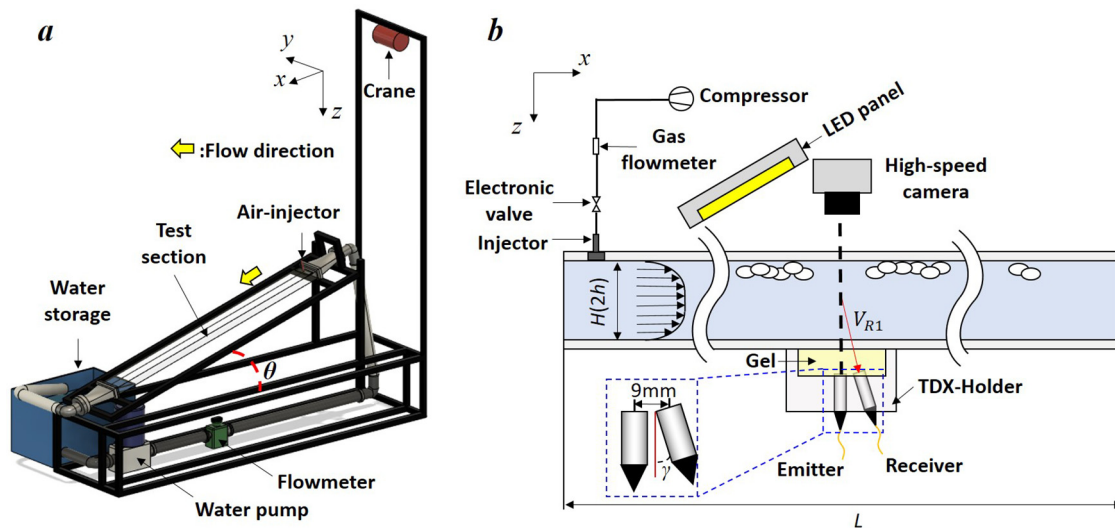


**FIG. 3.** Schematic diagram of the experimental setup. (a) Inclinable channel where the slope is set to a declined position as an example. (b) Details of the test section channel and the measurement system, where TDX indicates the transducer.

preamplifier (PR-60BP, Japan Probe Co., Ltd.) with a bandpass filter function to improve the signal-to-noise ratio, and its gain was maintained at +60 dB. The ultrasound signal obtained by the receiver was used to estimate the bubbly flow velocity profile, whereas the signal obtained by the transmitter was for the UPE measurement.

## B. Experimental conditions

The liquid flow rate was maintained at a constant value and checked by the electromagnetic flowmeter in all trials. The maximum bulk velocity ($U_{bulk}$) was estimated from the UVP results in single-phase flow (see the Appendix for details). The tilt angle $\theta$ was examined at 5° intervals in the range from −15° to 15°, and the bulk void fraction was 0.1%, estimated by the ratio of the air and liquid flow rates. The water temperature was approximately 24 °C, and the corresponding water density and kinematic viscosity were $\rho = 997$ kg/m$^3$ and $v = 1.0 \times 10^{-6}$ m$^2$/s, respectively. For the estimation of velocity profiles, tracer particles (CHP 20P/P120, Mitsubishi Chemical) with density $\rho_s = 1010$ kg/m$^3$ and mean diameter $d_s = 120$ $\mu$m were mixed into the water. The inertia of the particles can be evaluated by the Stokes number, $St = (\rho_s d_s 2\eta^{1/2})/(18\rho v3^{/2})$, where $\eta$ is the turbulent kinetic energy dissipation rate and $St$ is smaller than 0.09, indicating that the particles behave flow tracers. Note that $C_L$ of the bubble is affected by the degree of contamination.[38] Since almost bubbles float in the contaminated seawater for BDR, contaminated water is more suitable for the present study than pure water. For this reason, we utilized the groundwater existing in nature. This water quality is categorized to be well-contaminated water in which the hydrodynamic force of the bubbles is rather stabilized.[39,40] It is also noted that our team conducted similar experiments using silicon oil as the liquid phase to avoid the contamination effect previously.[41]

The spatial resolution of UPE is 29.6 $\mu$m ($\Delta\xi_{UPE} = 0.5c \times t_s$), and it is about 1/160 of the height of the sliding bubbles from the wall in the present study. Velocity profiles were estimated using 32 pulse signals to reconstruct one velocity profile, and 625 profiles ($N_{UVP}$) were acquired in 5 s. Therefore, the total number of echography profiles was 20 000. For the optical measurements, the frame rate and shutter speed are 1000 fps and 1/4000, respectively. Each image has a measurement area of $26 \times 29$ mm$^2$ and a resolution of 147 $\mu$m/pixel. Since data logger memory limitations, the maximum measurement time with a 40 ns sampling time is 5 s, the number of measured bubbles in a trial was not enough to analyze the bubble behavior statistically. Hence, ten measurement trials were carried out for each slope angle ($\theta$), so the corresponding total number of bubbles obtained for each $\theta$ was 120. The detailed experimental conditions are summarized in Table I.

An example of the optical and US combined measurements for the bubbly flow over 0.5 s is shown in Fig. 4. The equivalent diameter, $d_b = (4A_{proj}/\pi)^{1/2}$, where $A_{proj}$ is the projected bubble area, and the velocity ($u_b$) of each bubble were obtained from the optical measurement. The bubbles were detected by thresholding $d_b$ (>1 mm), i.e., tracer particles [the small dots in Fig. 4(a)] were excluded from the measurement. Figure 4(b) is the echography of bubbles passing through the emitter [TDX position in Fig. 4(a)] at a time synchronized with the optical system. The absolute value of the echo intensity ($I$) was normalized by the measurable voltage range ($V_{range}$) of the data logger (i.e., $I_{Norm.} = |I|/V_{range}$). Comparing the echography and time-line images [see labels b1–b5 in Figs. 4(a) and 4(b)] verifies adequate synchronization between the measurements. The maximum distance

**TABLE I.** Experimental conditions.

| Experimental conditions | |
|---|---|
| Measurement conditions | |
| Ultrasound frequency ($f_0$) | 4 MHz |
| Pulse repetition frequency ($f_{PRF}$) | 4 kHz |
| Cycles of ultrasound pulse | 4 |
| Sound speed (c) | 1480 m/s |
| Spatial resolution of UPE | 29.6 $\mu$m |
| Spatial resolution of UVP | 0.7 mm |
| Time resolution of UPE ($\Delta t_{UPE}$) | 0.25 ms |
| Time resolution of UVP ($\Delta t_{UVP}$) | 8 ms |
| Angles of receiver ($\gamma$) | 10° |
| Measurement time | 5 |
| The number of trials | 10 |
| | |
| Flow conditions | |
| $U_{bulk}$ | 0.75 m/s |
| Reynolds number ($Re = U_{bulk}h/v$) | 15 000 |
| Measurement point ($x/L$) | 0.6 |
| Inclination range of channel ($\theta$) | −15° to +15° |
| Void fraction (in channel bulk) | 0.1% |

between the wall and bottom of the bubble was defined as the bubble height ($h_b$) and was estimated by thresholding the normalized echo intensity. The liquid velocity ($u_l$) profiles were also estimated from the receiver, as shown in Fig. 4(c), where black masks indicate the bubble regions. The liquid velocity profiles in the bubble regions were excluded in evaluating the time-averaged velocity profile. The principles of US measurement are described in more detail in the Appendix.

## III. RESULTS AND DISCUSSION
## A. Qualitative visualization

The sliding motion of bubbles in the side view ($x$–$z$ plane) was visualized first to understand their behavior before the opto-acoustic measurement described in Sec. II was performed. A high-speed camera (FASTCAM Mini AX-50, PHOTRON Ltd.) and an LED panel were installed in front of and behind the channel, respectively, at $x/L = 0.6$. The frame rate and shutter speed were 2000 fps and 1/6000, respectively. Bubbles were injected intermittently with a syringe to observe individual motion by avoiding bubble swarm or coalescence. The bulk velocity of the liquid phase ($U_{bulk}$) was 0.85 m/s, corresponding to $Re = 17\,000$, and the slope angles were −10°, 0°, and 10°, corresponding to the declined, flat, and inclined conditions, respectively.

Time-series images of bubbles inside the turbulent channel flow are shown in Fig. 5. For the declined condition [Fig. 5(a)], the bubbles show periodic deformations through changes in their height. The bubble indicated by the red arrow has a sharp interface on the bottom with larger height at $t = 0.01$ s, becoming rounder with reduced height at $t = 0.02$ s. A decrease in the bubble height indicates an increase in the bubble length along the wall, seen by comparing the sliding motions at $t = 0.01$ s and 0.04 s. Periodic bubble deformation was observed in the declined condition but is not a distinctive feature in the flat [Fig. 5(b)] or inclined conditions [Fig. 5(c)]. We suppose that
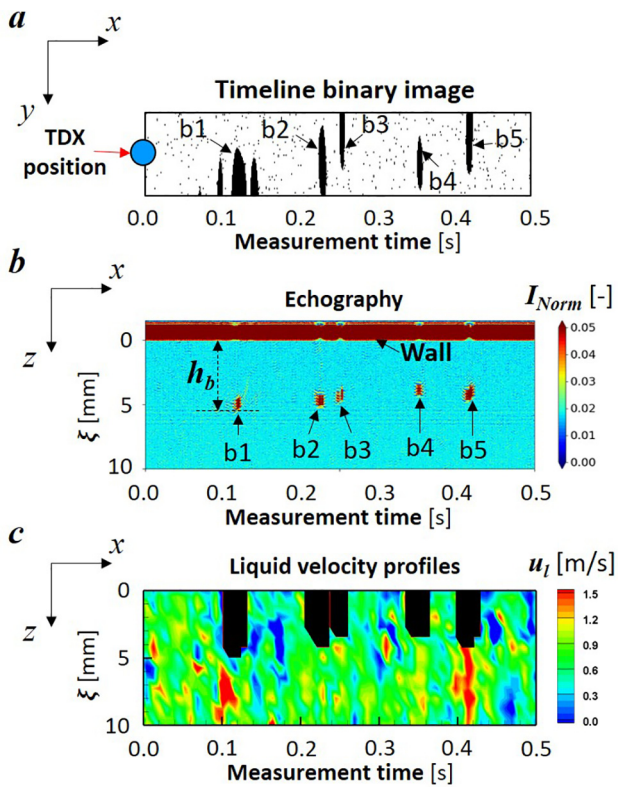
**FIG. 4.** Summary of optical and US measurements for the bubbly flow. (a) Timeline binary image and (b) echography in bubbly flow, where $\xi$ is the measurement distance. The region $\xi < 0$ mm is the top wall of the channel. (c) Liquid velocity profiles where the black masks are bubble regions. Data (a) were obtained from the optical measurement, whereas (b) and (c) were obtained from the US measurement.

the periodic deformation originates from the buoyancy and lift contributions. Because $F_{b,f}$ (in Fig. 1) acts on the bubble opposite to the inertia of liquid flow in the declined condition, the drag also increases, and the bubble length is instantaneously reduced. The bubble height then increases while maintaining a constant bubble volume. In this situation, the difference in the liquid velocity at the top and bottom of the bubble becomes larger. Therefore, the downward lift works to the bubble, and the height increases more due to the lift. In contrast, an upward lift can act on the bubble because of the velocity reversal between the bubble and the liquid phase flow (i.e., $u_b < u_l$). While the bubble height increases, the liquid velocity acting on the bubble also increases in the turbulent shear flow. The upward lift pushes the bubble toward the wall with $F_{b,w}$ (in Fig. 1), when the velocities of the bubble and liquid phase are reversed. The upward lift and $F_{b,w}$ cause a reduction in the bubble height without bubble fragmentation because of the surface tension contribution. In other words, the bubble volume is constant, and the bubble length increases while its height decreases. The bubbles under the declined condition slide near the wall, repeating these processes.

### B. Bubble velocity and height

Scatter plots of the advection velocity, $u_b$, and height, $h_b$, of bubbles vs the bubble diameter, $d_b$, for $\theta = -15°$, $0°$, and $15°$ are shown in Figs. 6(a) and 6(b), respectively. Dashed lines indicate the linear trends obtained by least squares fitting. The bubbles sliding on the inclined surface have higher velocities than those sliding under the flat surface, whereas the bubbles sliding under the declined surface have lower velocities than the flat surface. This is because the buoyancy ($F_{b,f}$ in Fig. 1) affects $u_b$. The bubbles are decelerated by the $F_{b,f}$ component in the declined condition while accelerated by the $F_{b,f}$ in the inclined condition. This trend is especially strong for the declined condition where $d_b$ increases due to the buoyancy effect, which is proportional to the bubble volume ($V_b = \pi d_b^2 h_b/6$).
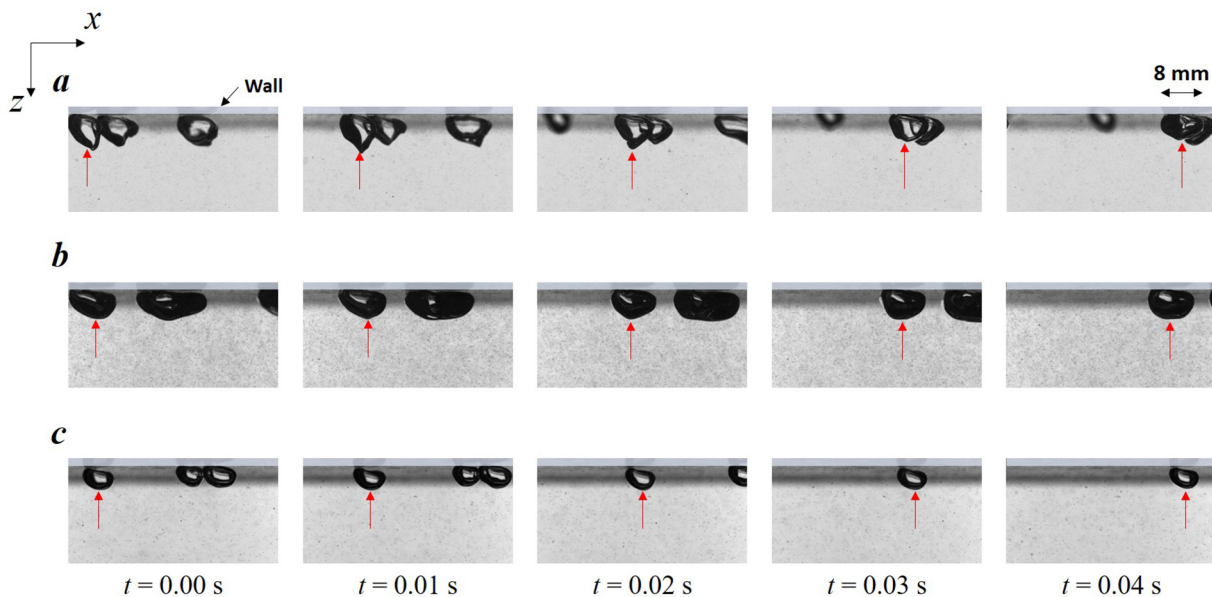


**FIG. 5.** Time-series images of bubbles for the qualitative visualization, where red arrows are the tracking indicators of the sliding bubble. (a) $\theta = -10°$, (b) $\theta = 0°$, and (c) $\theta = 10°$.
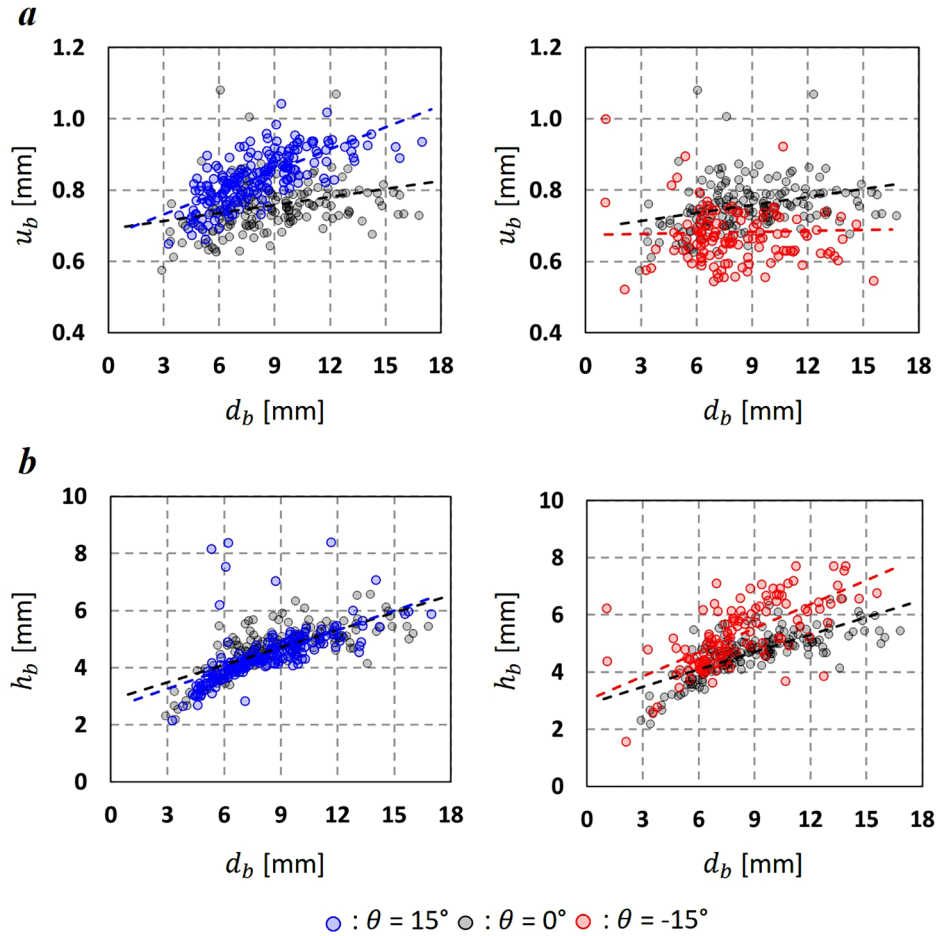
**FIG. 6.** Scatter plots of (a) bubble velocity $u_b$ and (b) bubble height $h_b$, vs bubble diameter $d_b$ for declined, flat, and inclined surfaces (corresponding to $\theta = -15°$, $0°$, and $15°$, respectively). Color dashed lines are linear fits.

The bubble height $h_b$ in the inclined condition shows a similar trend as the flat surface. The distribution of $h_b$ in the declined condition is wider than for the flat surface due to the periodic deformation of bubbles observed in the visualization Fig. 5(a). The repetition in the increase and decrease in $h_b$ in the declined condition is induced by the contribution of the buoyancy and lift, and the large distribution of $h_b$ values was obtained due to this repetition. In particular, $h_b$ in the declined condition increases more with increasing $d_b$ than for the other conditions [see trend lines in Fig. 6(b)]. Since bubble fragmentation was not observed in the optical measurements, it is concluded that the aspect ratio of bubbles changes instantaneously, maintaining a constant bubble volume. We expect that the lift coefficient changes with the aspect ratio.[10]

The mean velocity $(\bar{u}_b)$ and height $(\bar{h}_b)$ variations with $\theta$ are shown in Figs. 7(a) and 7(b), respectively. The mean velocity $\bar{u}_b$ increases monotonically with $\theta$. While $F_{b,f}$ acts on the bubble in the same direction as the inertia of the liquid flow in the inclined condition, it is the opposite in the declined condition. Since $F_{b,f}$ depends on $\theta$, the buoyancy effect increases with $\theta$. Namely, with an increase in the absolute inclination, $u_b$ in the declined condition tends to be reduced, whereas $u_b$ in the inclined condition tends to increase.

$F_{b,f}$ also influences $\bar{h}_b$ in the declined condition. $\bar{h}_b$ and its standard deviation increase with increasing $|\theta|$ in the declined condition. $\bar{h}_b$ varies more with $|\theta|$ when declined than when inclined. $F_{b,f}$ opposes the liquid flow inertia and increases with increasing $\theta$, as does the drag. For this reason, the bubble length along the wall is reduced, causing an increase in $h_b$. Simultaneously, a large downward lift acts on the bubble due to the increased velocity difference between the top and bottom of the bubble. Therefore, the lift contribution is instantaneously varied by $h_b$, and this variation results in the high standard deviation of $h_b$ in the declined condition. In contrast, the mean and standard deviation of $h_b$ do not change significantly for the inclined condition. Since $F_{b,f}$ acts on the bubble in the same direction with the inertia of liquid flow in the inclined condition, the drag induced by the inertia decreases. It causes that the bubble length does not decrease unlike the case of the declined condition, and $h_b$ also does not vary. As there is no large velocity difference between the top and bottom of the bubble without the variation of $h_b$, the large lift does not exert on the bubble as well. For this reason, there is no large variation of the bubble height in the inclined condition.

Figure 7(c) shows the time-averaged liquid velocity profiles in the bubbly flow at $\theta = -15°$, $0°$, and $15°$, where the vertical axis is a
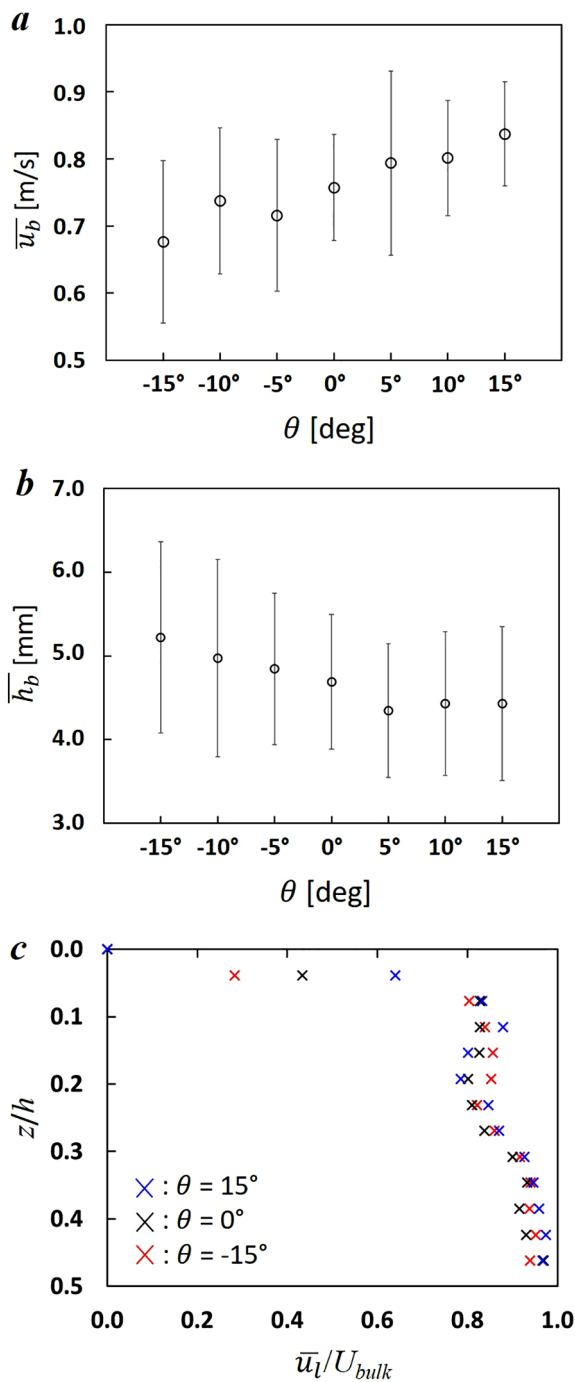
**FIG. 7.** Variation of (a) mean $u_b$ and (b) mean $h_b$ with $\theta$, where the error bars denote the standard deviation, and (c) time-averaged velocity profiles in the bubbly flow at $\theta = -15°$, $0°$, and $15°$.

vertical distance from the top wall of the channel normalized by the channel half-height. $\overline{ul}$ near the wall ($z/h < 0.10$) is smaller in the declined condition than in the other conditions. This is because $u_l$ near the bubble decreases when $F_{b,f}$ acts on the bubble opposite to the liquid flow in the declined condition. However, for the inclined condition, $\overline{ul}$ is larger than for that of the other conditions due to the contribution of $F_{b,f}$.

## C. Lift coefficient of bubbles

The lift generally contributes to the lateral migration of bubbles, and stick-slip bubbles can be observed in slow-speed bubbly flow or sliding bubbles along hydrophobic walls governed by drag and lift.[42,43] However, in the case of millimeter-sized bubbles in a turbulent channel flow, it can cause variations in $h_b$ rather than lateral migration due to strong turbulent intensity. The liquid velocity acting on the bubble increases while the downward lift increases bubble height. The upward lift begins to act on the bubble because of the velocity alternation between the liquid phase and bubbles before the bubbles migrate laterally. Because the upward lift pushes the bubble toward the wall with force $F_{b,w}$, the bubble height is reduced. This mechanism causes the height to vary periodically without lateral migration, as shown in Fig. 5. Therefore, we adopted a force balance equation on stationary bubbles in the downward vertical direction to estimate the lift coefficient of bubbles.

### 1. Force balance equation

In the experiment, we confirmed the variation of $h_b$ with $\theta$, and the large standard deviation of $h_b$ was significant in the declined condition. We analyze the lift coefficient of the bubbles to elucidate the $h_b$ variation mechanism. Although there is no universal lift model applicable to turbulent shear flow, Auton's lift model[5] is the most acceptable, because it is based on inertial effects. That is, the velocity difference between the top and bottom of the bubble causes a lateral pressure difference on the bubble surface. Auton's model is more physically suitable than the Magnus lift based on fluid circulation around an object or Saffman's lift model based on viscous effects.[44] Hence, this work employs a lift model following Auton's inertia lift formulation, as described by

$$F_L = C_L \rho V_b \omega (u_b - u_l), \quad \left( V_b = \frac{1}{6}\pi d_b^2 h_b, \; \omega = \frac{\partial u_l}{\partial z} \right), \quad (1)$$

where $V_b$ is the bubble volume and $\omega$ is the velocity gradient intensity. The upper surface of bubbles leaves a thin liquid film as shown in Fig. 5, and it causes asymmetric deformation of bubbles in the wall-normal direction, originally due to the pressure increase inside the liquid film. Although the pressure increase inside the liquid film cannot be measured experimentally, it can be estimated by the curvature of the bubble interface from the optical measurement. It is, thus, $F_{b,w}$ and the surface tension ($F_s$) corresponding to the pressure increase were considered in balancing the lift, where $F_{b,w}$ is the buoyancy component normal to the wall, as illustrated in Fig. 1. Note that the surface tension does not contribute to the translational force of the bubble directly, but it first contributes to the deformation, and then $C_L$ changes due to the deformation. The modeling of the surface tension is shown in Fig. 8.

In Fig. 8, R1 denotes the bubble bottom radius of curvature, which surface the tension acts on, and R2 and R3 indicate the curvature radii of each side. $\varepsilon$ is the liquid film thickness, and $\theta_s$ is the working angle of the surface tension on the side curvatures. The surface tension equation can be expressed as follows:
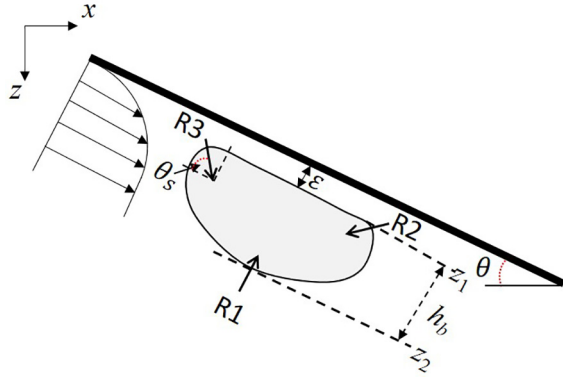
**FIG. 8.** Sketch of the surface tension acting on a bubble. R1 is the bubble bottom radius of curvature, while R2 and R3 are the side curvature radii. $\theta_s$ is the angle of R2 and R3, and $\varepsilon$ is the liquid film thickness.

$$F_s = \sigma \left( \frac{S_2 \cos \theta_{s2}}{R2} + \frac{S_3 \cos \theta_{s3}}{R3} - \frac{S_1}{R1} \right), \quad (2)$$

where $S_1$, $S_2$, and $S_3$ are the areas on which the surface tension works on the bottom and two side curvatures, respectively, and $\sigma$ is the surface tension, equal to $\sigma = 0.073$ N/m for pure water. There are four assumptions used to establish the force balance equation:

(i)  Because it is difficult to estimate the radii of both side curvatures, we assumed that these radii are equal, i.e., R2 = R3 (implying that $S_2 = S_3$). This assumption can be supported by the qualitative visualization (Fig. 5) that the side curvatures for many bubbles are similar, even though the sides have slightly different shapes at each instant in time.

(ii) The surface tension acts on the side curvature of the bubble at a 45° angle, i.e., $\theta_{s2} = 45°$.

(iii) $\varepsilon$ is negligible compared with $h_b$. This assumption is reasonable because the scale of $\varepsilon$ is micrometers[31] while the scale of $h_b$ is millimeters, as shown in Fig. 7(b). Then, the velocity gradient from the bottom to the top of the bubble is $\omega = (u_{l,z2} - u_{l,z1})/(z_2 - z_1)$, where $z_1$ and $z_2$ are the distances from the bubble top and bottom to the wall as shown in Fig. 8. This can be simplified to $\omega = u_{l,z2}/h_b$ using the no-slip condition ($u_{l,z1} = 0$) based on this assumption ($z_1 = 0$).

(iv) R1 and R2 (= R3) are about a half of $d_b$ and $h_b$, respectively, i.e., R1 = $d_b/2$, R2 = R3 = $h_b/2$. The corresponding $S_1$ and $S_2$ (= $S_3$) are $(\pi d_b 2)/4$ and $(\pi d_b h_b)/4$, respectively.

With the above assumptions, Eq. (2) can be rewritten as

$$F_s = \sigma \left( \frac{2S_2 \cos \theta_{s2}}{R2} - \frac{S_1}{R1} \right) = \sigma \left( \frac{\sqrt{2}}{2} \pi d_b - \frac{1}{2} \pi d_b \right)$$
$$= \frac{\pi \sigma}{2} d_b \left( \sqrt{2} - 1 \right). \quad (3)$$

The errors in the above assumptions will be evaluated by estimating surface tension next.

The equation for the force balance among the lift, buoyancy, and surface tension can be expressed as Eq. (4), and the lift coefficient is consequently estimated from Eq. (5)

$$C_L \rho V_b \omega (u_b - u_l) + \frac{\pi \sigma}{2} d_b \left( \sqrt{2} - 1 \right) - \rho g V_b \cos \theta = 0, \quad (4)$$

$$C_L = \frac{-\frac{\pi \sigma}{2} d_b (\sqrt{2} - 1) + \rho g \frac{1}{6} d_b^2 h_b \cos \theta}{\rho \frac{1}{6} d_b^2 h_b \omega (u_b - u_l)},$$

$$C_L = \frac{\frac{3\sigma}{d_b h_b} (1 - \sqrt{2}) + \rho g \cos \theta}{\rho \omega (u_b - u_l)}. \quad (5)$$

The measurement of the variables on the right-hand side of Eq. (5) gives the lift coefficient for given conditions of the inclination angle $\theta$. Three dimensionless numbers were adopted to parameterize $C_L$ in terms of the spherical-volume equivalent bubble diameter, $d_{eq} = (d_b^2 h_b)^{1/3}$. One parameter is the bubble Reynolds number $Re_b$, representing the flow field around the bubble

$$Re_b = \frac{|u_b - u_l| d_{eq}}{\nu}, \quad (6)$$

and another is the Weber number $We$, representing the bubble deformation

$$We = \frac{\rho (u_b - u_l)^2 d_{eq}}{\sigma}. \quad (7)$$

The final parameter is the Bond number $Bo$, representing the bubble shape

$$Bo = \frac{\rho g d_{eq}^2}{\sigma}. \quad (8)$$

$C_L$ obtained from Eq. (5) was first classified by the aspect ratio of the bubble ($\chi = d_b/h_b$, $\chi > 1$) into bins of $\pm 0.5$ and plotted with $Bo$, $We$, and $Re_b$ numbers, respectively. The liquid velocity $u_l$ acting on the bubble is estimated by averaging all liquid velocities acting on the bubble from the bottom to the top of the bubble. These results will be discussed next.

### 2. Modeling of lift coefficient

Scatter plots of the bubble lift coefficient, $C_L$, vs the dimensionless numbers, $Bo$, $We$, and $Re_b$ are shown in the log-log plots of Fig. 9. We categorized $C_L$ by $\chi$ because it is likely that $C_L$ is affected by $\chi$. $C_L$ increases with increasing $Bo$ as shown in Fig. 9(a). $Bo$ indicates the ratio between buoyancy and surface tension. The bubble becomes flat and fat when buoyancy is more dominant than surface tension and has a spherical shape when $Bo \approx 1$. Accordingly, spherical bubbles have low $C_L$, while the flat-fat bubbles have high $C_L$. In contrast, $C_L$ decreases with increasing $We$ and $Re_b$ as shown in Figs. 9(b) and 9(c). This trend is similar to rising deformable bubbles in a linear shear flow.[9] A striking feature of these graphs is that $C_L$ distributions are widely scattered for all $\chi$, implying that the dimensionless numbers alone cannot be used to characterize the bubble behavior. We, thus, combined those numbers considering $\chi$ in modeling the lift coefficient of wall-sliding bubbles.

Based on the results as discussed above, two formulas that are applicable to the certain range of the Reynolds number, $10^1 < Re_b < 10^5$, were derived to predict $C_L$ as follows:

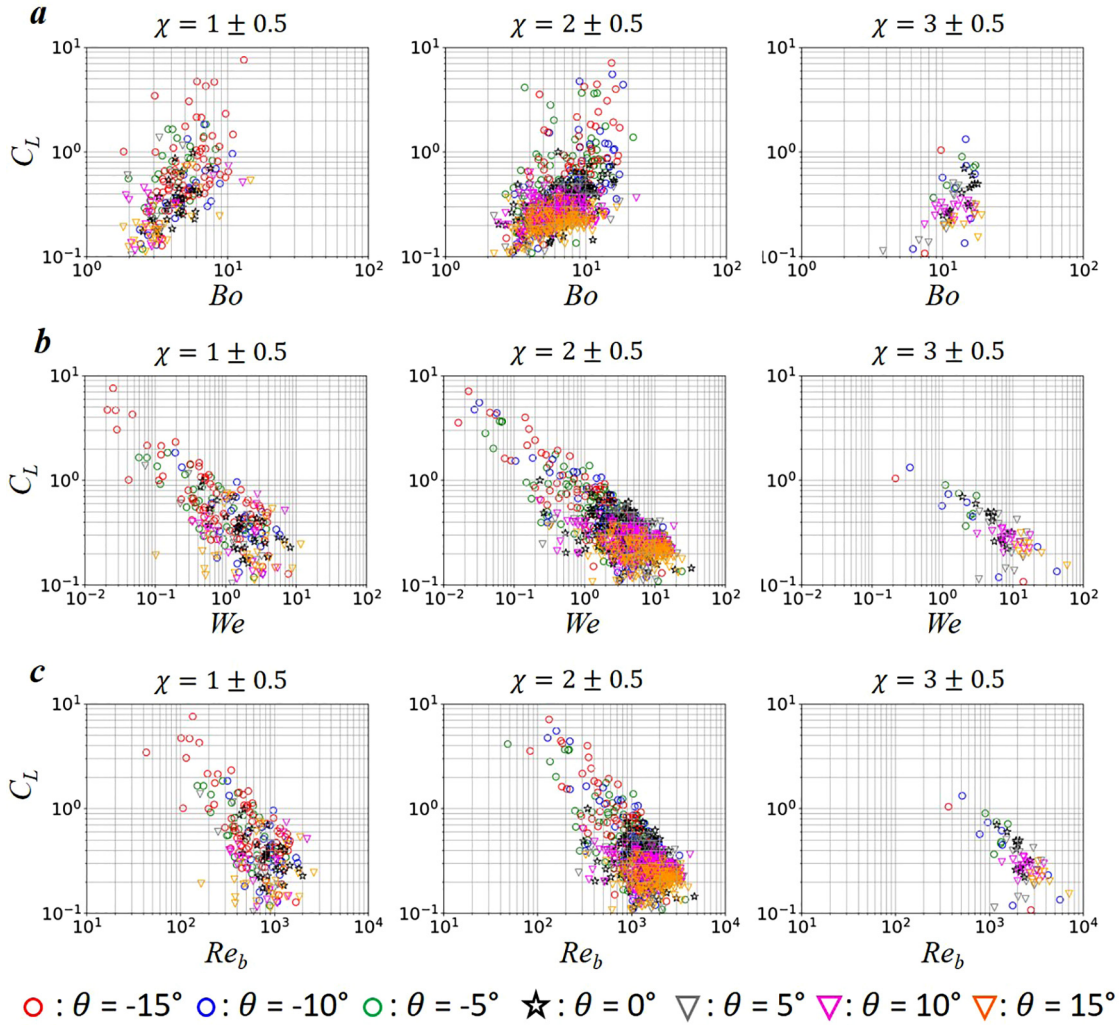$$C_L = \frac{\alpha(\chi) Bo}{\sqrt{We}}, \quad (9)$$

FIG. 9. Scatter plots of the lift coefficient $C_L$ vs (a) Bo, (b) We, and (c) Re. The symbols represent the slope conditions.

$$C_L = \frac{\beta(\chi) Bo}{Re_b}, \qquad (10)$$

where $\alpha(\chi)$ and $\beta(\chi)$ are dimensionless functions of $\chi$. Figures 10(a) and 10(b) show comparisons of the measured $C_L$ and the modeled $C_L$ using Eqs. (9) and (10), respectively, for each $\chi$. The color and shape of the symbols denote the inclination angles. Although the modeled $C_L$ shows slight scatter from a perfect correlation (black line in graphs), most $C_L$ values nearly match the measured lift coefficient. The average absolute percentage error (AAPE) was evaluated as

$$\text{AAPE} = \frac{1}{n} \sum_{n=1}^{n} \frac{|C_{L,\text{experiment}} - C_{L,\text{predicted}}|}{C_{L,\text{experiment}}} \times 100 \, [\%], \qquad (11)$$

where $n$ is the number of bubbles and the results are summarized in Table II. We suppose that the errors primarily originate from the high turbulence rather than the bubble motion dependent contamination affecting the instability of $C_L$.[45] This is because the contamination

effect is overshadowed by large stochastic components of the bubble shape and deformation due to the turbulence as shown in Fig. 9.

The errors tend to be reduced with increasing $\chi$, and the error for Eq. (9) is lower than Eq. (10). Therefore, the ratio of $We$ and $Bo$ more suitably models $C_L$ than the ratio of $Re_b$ and $Bo$, which signifies that $C_L$ depends strongly on the deformation and shape of the bubble.

The factors $\alpha$ and $\beta$ estimated for each $\chi$ using a least squares fit are plotted as a function of $\chi$ in Fig. 11. The two solid curves are the results of the least squares fit functions of $\alpha$ and $\beta$, respectively, and the fitting equations are given as

$$\alpha(\chi) = -0.0076\chi^2 + 0.0106\chi + 0.097, \quad 1 < \chi \le 3, \qquad (12)$$
$$\beta(\chi) = -6.3\chi^2 + 14.3\chi + 64.9, \quad 1 < \chi \le 3. \qquad (13)$$

The applicability of the functions for $\chi > 1$ means that the case of a spherical bubble is excluded. Note that $\chi = 1$ is an exception because we categorized $\chi$ with integer values. $\alpha$ and $\beta$ are reduced with an increase in $\chi$.
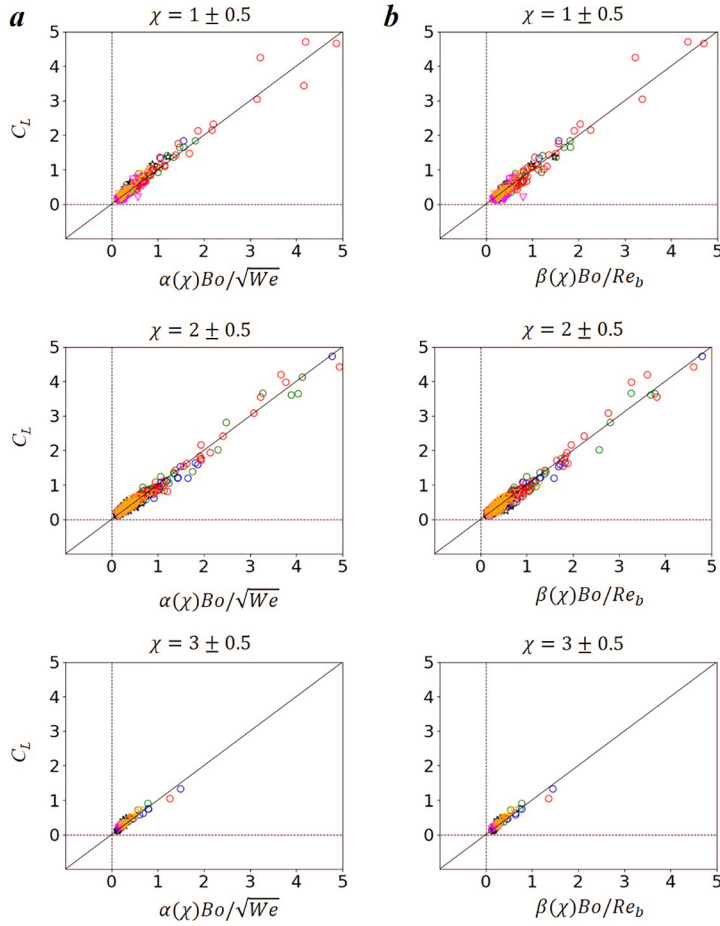
**FIG. 10.** Comparison of measured $C_L$ vs the predictions of (a) Eq. (9) in the left side graphs and (b) Eq. (10) in the right side graphs. Vertical axes are $C_L$ obtained from Eq. (5), while horizontal axes mean $C_L$ estimated from Eqs. (9) and (10). The symbols represent the slope conditions. Black lines indicate a perfect correlation.

$\bigcirc : \theta = -15°$ $\bigcirc : \theta = -10°$ $\bigcirc : \theta = -5°$ $\bigstar : \theta = 0°$ $\triangledown : \theta = 5°$ $\triangledown : \theta = 10°$ $\triangledown : \theta = 15°$

Equation (9) is used for the estimation of lift, and the mean forces acting on the bubbles are calculated for further analysis of bubble deformation as shown in Fig. 12 for (a) $\theta = -15°$, (b) $\theta = 0°$, and (c) $\theta = 15°$ using $d_{eq}$. The red, black, and blue symbols indicate the lift, surface tension, and buoyancy, respectively. The horizontal and vertical error bars show the standard deviations of $d_{eq}$ and the forces. The surface tension is roughly 10%–20% of the buoyancy, and this indicates that the bubble deformation is primarily governed by the lift and buoyancy contribution. A striking feature is that the standard deviations of the lift at $\theta = -15°$ are much larger than those of the other conditions because of the periodic bubble deformation in the declined

**TABLE II.** AAPE of Eqs. (9) and (10) for each $\chi$.

| $\chi$ | $n$ | AAPE of Eq. (9) (%) | AAPE of Eq. (10) (%) |
|---|---|---|---|
| 1 | 223 | 16 | 27 |
| 2 | 798 | 13 | 17 |
| 3 | 70 | 12 | 13 |



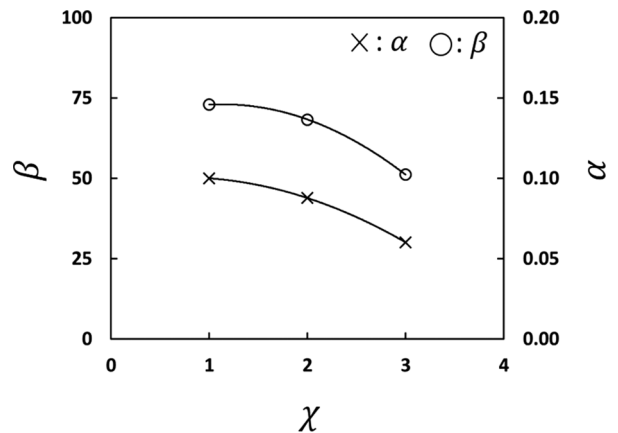**FIG. 11.** Factors $\alpha$ (right vertical axis) and $\beta$ (left vertical axis) of Eqs. (9) and (10) vs the bubble aspect ratio $\chi$. Solid curves are the least-square fits, Eqs. (12) and (13).
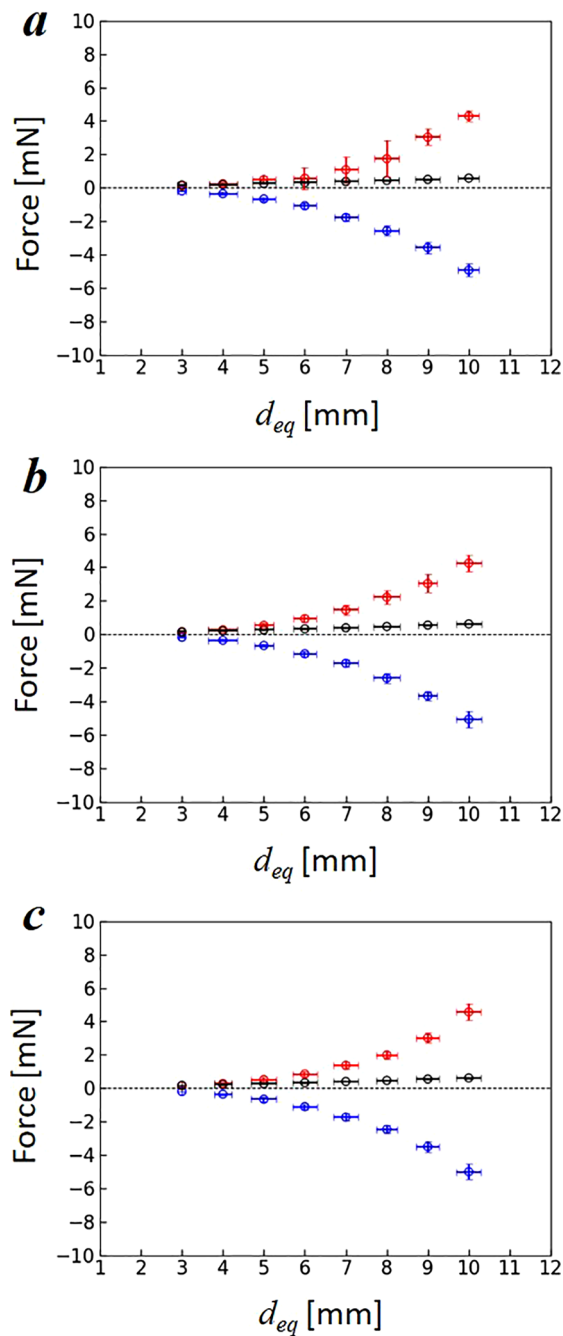
**FIG. 12.** Forces acting on the bubble perpendicular to the wall using the volume-spherical equivalent diameter, $d_{eq}$, at (a) $\theta = -15°$, (b) $\theta = 0°$, and (c) $\theta = 15°$. The red, blue, and black symbols indicate the lift, buoyancy, and surface tension, respectively. Horizontal and vertical error bars indicate the standard deviations of $d_{eq}$ and forces.

## IV. CONCLUSIONS

We experimentally investigated the behavior of bubbles sliding along a wall subject to turbulent boundary layers in an inclinable channel with tilt angles ranging from $-15°$ to $15°$. An opto-acoustic combined measurement technique was utilized. Liquid velocity profiles and bubble heights from the wall were obtained by the ultrasound pulse Doppler method, and the diameter and velocity of individual bubbles were obtained from PTV image processing. About 1000 bubbles were detected in the experiment to take statistics, targeting the range of bubble diameter from 2 to 18 mm. Our conclusions are as follows:

1. Compared with the bubble velocity under the flat condition, the velocity decreased by up to 10% for the negative slope condition while increasing by up to 10% for the positive slope condition as a result of the buoyancy effect. In addition to velocity, periodic deformations of bubbles were observed in the visualizations for the negative slope condition but were not observed for the flat and inclined conditions. Because of the periodic deformation, the bubble height from the wall increases by 3%–10% compared with the flat condition with an increasing absolute inclination in the negative slope condition. The increase in the bubble height is intensified with an increasing inclination of the declined surface.

2. The lift coefficient of the bubble, $C_L$, was estimated from the force balance among lift, surface tension, and buoyancy using measured quantities from the experiment. $C_L$ was defined using Auton's inertia lift formulation and modeled using two functions with either the $We$ or $Re_b$ number as the primary dimensionless parameter. The $Bo$ number and aspect ratio $\chi$ were used as secondary dimensionless parameters in both functions. It is more reasonable to use the model based on $We$ to predict $C_L$ than $Re_b$, because the error of the $We$-based model was up to 10% less than that of the $Re_b$-based model. This implies that $C_L$ is governed by bubble deformation in the turbulent channel flow. Moreover, it can be concluded that the bubble shape has a significant effect on $C_L$ because it changes with the aspect ratio $\chi$.

The deformation and thickness of the liquid film are important characteristics to determine the efficiency of BDR,[30,31,46] and the information on $C_L$ is required to predict them in the turbulent boundary layers. We expect that the proposed correlations for $C_L$ will be useful information to predict them in the numerical study. We will also investigate the structure of turbulent boundary layers affected by the deformation in the future work.

## AUTHOR DECLARATIONS
### Conflict of Interest

The authors have no conflicts to disclose.

### DATA AVAILABILITY

The data that support the findings of this study are available within the article.

condition. A large lift acts on the bubble as the bubble height increases, and the lift decreases with a reduction in the bubble height. Because periodic deformations were not observed for the flat and inclined conditions, the deviations in the lift are smaller than for the declined condition.

## APPENDIX: ULTRASOUND MEASUREMENT TECHNIQUE

Fluid phases based on the echo intensity can be determined, because the intensity reflected by a medium relies on its acoustic impedance.[47] To identify a bubbly flow gas-phase interface, the echography was first obtained in the single-phase flow, as shown in Fig. 13(a). The absolute value of the echo intensity was normalized by the measurable voltage range ($V_{range}$) of the data logger (i.e., $I_{Norm.} = |I|/V_{range}$). In the range of $10\,mm < \xi < 40\,mm$, it is well-known that there are echoes of multiple reflections when using UVP. The multi-reflection of ultrasound waves from the wall is inevitable when emitting ultrasound in a limited range along a measurement line, and this problem also causes erroneous velocity data. It was confirmed that most bubbles slide within the range $0\,mm < \xi < 10\,mm$, so we adjusted the TDX emitter settings to prevent the echo of multiple reflections in this range, defined as the region of interest (ROI) for the US measurement. The number of echo signals obtained by the emitter in the ROI over 5 s is $6.08 \times 10^6$, and the intensity distribution was analyzed using a probability density function (PDF) as shown in Fig. 13(b). The threshold intensity

value of the particles is determined using statistical information. Thus, the threshold value was set to 0.03 because 99.9% of the particle intensities of particles that existed were in the range of $I_{Norm} < 0.03$. Therefore, the bubble interfaces were identified as being above this threshold value.

The UVP technique was utilized to estimate the liquid velocity profiles. Figure 14(a) shows the transducer configuration. The yellow region is the area of the emitted ultrasound beam. Black dashed and dotted lines are the measurement and reflected lines, respectively. $\theta_r$ means the angle between the measured and reflected lines for each measurement distance. Angles $A$ and $B$ indicate the angle between the measurement line and velocity magnitude $V$ [$=(u^2 + w^2)^{1/2}$] and the angle between the reflected line and $V$, respectively. With this configuration, the Doppler equation becomes

$$f_d = \frac{f_0 V(\cos A + \cos B)}{c} = \frac{f_0 V(\cos A + \cos(A - \theta_r))}{c}, \quad (A1)$$

where $f_d$ is the Doppler frequency obtained from the receiver. Because it is likely that the time-averaged velocities in the spanwise ($v$) and vertical-downward ($w$) directions converge to zero in the turbulent flow, we can assume that $V$ converges to the streamwise velocity ($u_l$). Then, the angle $A$ becomes 90°, and Eq. (A1) can be rewritten as

$$f_d = \frac{f_0 u_l}{c} \sin \theta_r,$$
$$u_l = \frac{c f_d}{f_0} \frac{1}{\sin \theta_r} = \frac{2 V_R}{\sin \theta_r}, \quad \left(V_R = \frac{c f_d}{2 f_0}\right), \quad (A2)$$

where $V_R$ is the velocity estimated by $f_d$ obtained from the receiver.

In a previous US measurement study,[48] multiple conventional transducers were set on a measurement line with one acting as the emitter and the others as receivers. It was confirmed that a measurable distance is determined by the receiver angle and the distance between the emitter and receiver. In the study, $\theta_r$ is always constant in the measurable distance and the same as $\gamma$. Accordingly, Eq. (A2) can be rewritten as
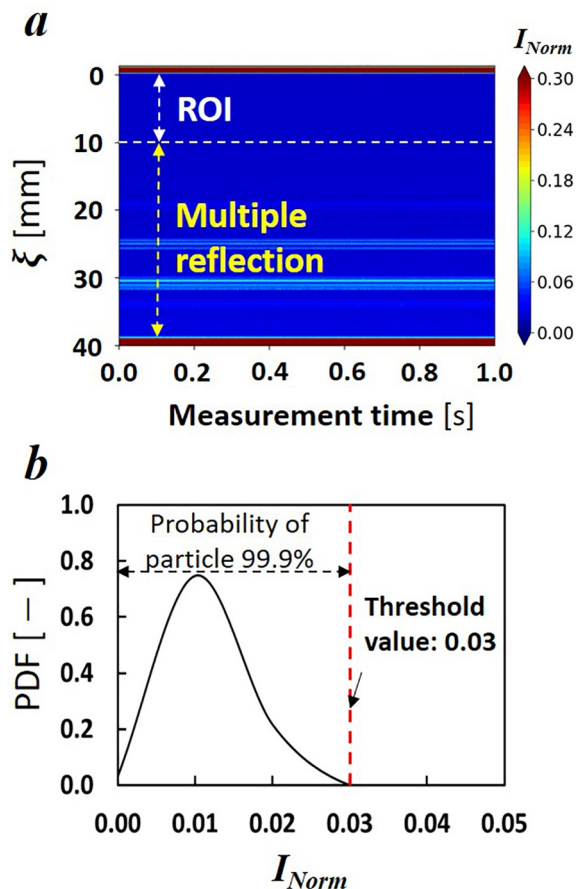


**FIG. 13.** The echo signal information in the single-phase flow. (a) Location of the region of interest (ROI) in the echography and (b) probability density function (PDF) of the normalized intensity reflected by the particles in the ROI.
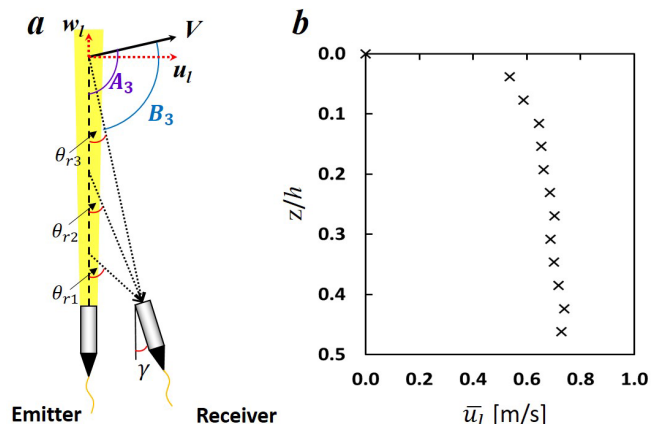


**FIG. 14.** UVP system configuration and results. (a) Principle of velocity profiling using two transducers and (b) time-averaged liquid velocity profile for $\theta = 0°$ obtained by the US measurement in a single-phase flow.

$$u_l = \frac{2V_R}{\sin\gamma}. \tag{A3}$$

The liquid velocity profiles were estimated using Eq. (A3). A quadrature-phase demodulation[49] and an autocorrelation method[50] were applied to the receiver echo signal to extract $f_d$ from the raw echo signals. Figure 14(b) shows the time-averaged velocity profile measured at the same time as the echography in Fig. 13(a). $U_{bulk}$ was estimated as the maximum velocity in the ROI, corresponding to $U_{bulk} = 0.75$ m/s.

## REFERENCES

[1] I. Žun, "The transverse migration of bubbles influenced by walls in vertical bubbly flow," Int. J. Multiphase Flow **6**, 583–588 (1980).

[2] M. Bertodano, R. T. Lahey, and O. C. Jones, "Phase distribution in bubbly two-phase flow in vertical ducts," Int. J. Multiphase Flow **20**, 805–818 (1994).

[3] W. C. Sanders, E. S. Winkel, D. R. Dowling, M. Perlin, and S. L. Ceccio, "Bubble friction drag reduction in a high-Reynolds-number flat-plate turbulent boundary layer," J. Fluid Mech. **552**, 353–380 (2006).

[4] B. R. Elbing, S. S. Mäkiharju, A. Wiggins, M. Perlin, D. R. Dowling, and S. L. Ceccio, "On the scaling of air layer drag reduction," J. Fluid Mech. **717**, 484–513 (2013).

[5] T. R. Auton, "The lift force on a spherical body in a rotational flow," J. Fluid Mech. **183**, 199–218 (1987).

[6] D. Legendre and J. Magnaudet, "The lift force on a spherical bubble in a viscous linear shear flow," J. Fluid Mech. **368**, 81–126 (1998).

[7] A. Tomiyama, H. Tamai, I. Žun, and S. Hosokawa, "Transverse migration of single bubbles in simple shear flows," Chem. Eng. Sci. **57**, 1849–1858 (2002).

[8] R. Adoua, D. Legendre, and J. Magnaudet, "Reversal of the lift force on the oblate bubble in a weakly viscous linear shear flow," J. Fluid Mech. **628**, 23–41 (2009).

[9] S. Aoyama, K. Hayashi, S. Hosokawa, D. Lucas, and A. Tomiyama, "Lift force acting on single bubbles linear shear flows," Int. J. Multiphase Flow **96**, 113–122 (2017).

[10] W. Lee and J. Lee, "Experiment and modeling of lift force acting on single high Reynolds number bubbles rising in linear shear flow," Exp. Therm. Fluid Sci. **115**, 110085 (2020).

[11] H. Hessenkemper, T. Ziegenhein, R. Rzehak, D. Lucas, and A. Tomiyama, "Lift force coefficient of ellipsoidal single bubbles in water," Int. J. Multiphase Flow **138**, 103587 (2021).

[12] H. Hessenkemper, T. Ziegenhein, D. Lucas, and A. Tomiyama, "Influence of surfactant contaminations on the lift force of ellipsoidal bubbles in water," Int. J. Multiphase Flow **145**, 103833 (2021).

[13] K. Hayashi, H. Hessenkemper, D. Lucas, D. Legendre, and A. Tomiyama, "Scaling of lift reversal of deformed bubbles in air–water systems," Int. J. Multiphase Flow **142**, 103653 (2021).

[14] W. Xu, S. Li, L. Pan, and Z. Li, "Experimental investigation about the lift force of a single bubble in the water at a linear shear flow," Int. J. Multiphase Flow **145**, 103819 (2021).

[15] M. E. McCormick and R. Bhattacharyya, "Drag reduction of a submersible hull by electrolysis," Nav. Eng. J. **85**, 11–16 (1973).

[16] N. K. Madavan, S. Deutsch, and C. L. Merkle, "Reduction of turbulent skin friction by microbubbles," Phys. Fluids **27**, 356–363 (1984).

[17] N. K. Madavan, S. Deutsch, and C. L. Merkle, "Measurement of local skin friction in a microbubble modified turbulent boundary layer," J. Fluid Mech. **156**, 237–256 (1985).

[18] X. Shen, S. L. Ceccio, and M. Perlin, "Influence of bubble size on micro-bubble drag reduction," Exp. Fluids **41**, 415–424 (2006).

[19] J. Lu, A. Fernández, and G. Tryggvason, "The effect of bubbles on the wall drag in a turbulent channel flow," Phys. Fluids **17**, 095102 (2005).

[20] Y. Murai, Y. Oishi, Y. Tasaka, and F. Yamamoto, "Turbulent shear stress profiles in a bubbly channel flow assessed by particle tracking velocimetry," Exp. Fluids **41**, 343–352 (2006).

[21] H. J. Park, Y. Tasaka, Y. Oishi, and Y. Murai, "Drag reduction promoted by repetitive bubble injection in turbulent channel flows," Int. J. Multiphase Flow **75**, 12–25 (2015).

[22] T. Tanaka, H. J. Park, Y. Tasaka, and Y. Murai, "Spontaneous and artificial void wave propagation beneath a flat-bottom model ship," Ocean Eng. **214**, 107850 (2020).

[23] X. Zhang, J. Wang, and D. Wan, "Euler–Lagrange study of bubble drag reduction in turbulent channel flow and boundary layer flow," Phys. Fluids **32**, 027101 (2020).

[24] S. L. Ceccio, "Friction drag reduction of external flows with bubble and gas injection," Annu. Rev. Fluid Mech. **42**, 183–203 (2010).

[25] Y. Murai, "Frictional drag reduction by bubble injection," Exp. Fluids **55**, 1773 (2014).

[26] Y. Kodama, A. Kakugawa, T. Takahashi, and H. Kawashima, "Experimental study on microbubbles and their applicability to ships for skin friction reduction," Int. J. Heat Fluid Flow **21**, 582–588 (2000).

[27] S. Mizokami, M. Kawakado, M. Kawano, T. Hasegawa, and I. Hirakawa, "Implementation of ship energy-saving operations with Mitsubishi air lubrication system," MHI Tech. Rev. **50**, 44–49 (2013).

[28] I. Kumagai, Y. Takahashi, and Y. Murai, "Power-saving device for air bubble generation using a hydrofoil to reduce ship drag: Theory, experiments, and application to ships," Ocean Eng. **95**, 183–194 (2015).

[29] Y. Murai, H. Fukuda, Y. Oishi, Y. Kodama, and F. Yamamoto, "Skin friction reduction by large air bubbles in a horizontal channel flow," Int. J. Multiphase Flow **33**, 147–163 (2007).

[30] A. Kitagawa, K. Hishida, and Y. Kodama, "Flow structure of microbubble-laden turbulent channel flow measured by PIV combined with the shadow image technique," Exp. Fluids **38**, 466–475 (2005).

[31] H. J. Park, Y. Tasaka, and Y. Murai, "Bubbly drag reduction investigated by time-resolved ultrasonic pulse echography for liquid films creeping inside a turbulent boundary layer," Exp. Therm. Fluid Sci. **103**, 66–77 (2019).

[32] C. Kawakita and T. Hamada, "Experimental investigation on influence of inclination and curved surface of ship bottom in air lubrication method," in Proceeding of the ASME-JSME-KSME (ASME, 2019).

[33] T. Maxworthy, "Bubble rise under an inclined plate," J. Fluid Mech. **229**, 659–674 (1991).

[34] H. K. Tsao and D. L. Koch, "Observations of high Reynolds number bubbles interacting with a rigid wall," Phys. Fluids **9**, 44 (1997).

[35] C. Barbosa, D. Legendre, and R. Zenit, "Conditions for the sliding-bouncing transition for the interaction of a bubble with an inclined wall," Phys. Rev. Fluids **1**, 032201 (2016).

[36] H. J. Park, Y. Tasaka, and Y. Murai, "Ultrasonic pulse echography for bubbles traveling in the proximity of a wall," Meas. Sci. Technol. **26**, 125301 (2015).

[37] Y. Takeda, "Development of an ultrasound velocity profile monitor," Nucl. Eng. Des. **126**, 277–284 (1991).

[38] M. Rastello, J. Mari, N. Grosjean, and M. Lance, "Drag and lift forces on interface-contaminated bubbles spinning in a rotating flow," J. Fluid Mech. **624**, 159–178 (2009).

[39] A. Tomiyama, I. Kataoka, I. Zun, and T. Sakaguchi, "Drag coefficients of single bubbles under normal and micro gravity conditions," JSME Int. J., Ser. B. **41**, 472 (1998).

[40] A. Tomiyama, G. P. Celata, S. Hosokawa, and S. Yoshida, "Terminal velocity of single bubbles in surface tension force dominant regime," Int. J. Multiphase Flow **28**, 1497–1519 (2002).

[41] Y. Oishi, Y. Murai, and Y. Tasaka, "Wall shear stress modified by bubbles in a horizontal channel flow of silicone oil in the transition region," Int. J. Heat Fluid Flow **86**, 108748 (2020).

[42] A. Kitagawa, P. Denissenko, and Y. Murai, "Behavior of bubbles moving along horizontal flat plates with different surface wettability," Exp. Therm. Fluid Sci. **104**, 141–152 (2019).

[43] A. Kitagawa, P. Denissenko, and Y. Murai, "Entrapment and cross-flow transport of air bubbles by a hydrophobic strip in a turbulent channel flow," Exp. Fluids **62**, 198 (2021).

[44] P. G. Saffman, "The lift on a small sphere in a slow shear flow," J. Fluid Mech. **22**, 385–400 (1965).

[45] S. Takagi and Y. Matsumoto, "Surfactant effects on bubble motion and bubbly flows," Annu. Rev. Fluid Mech. **43**, 615–636 (2011).

[46] K. Fukagata, K. Iwamoto, and N. Kasagi, "Contribution of Reynolds stress distribution to the skin friction in wall-bounded flows," Phys. Fluids **14**, L73 (2002).

[47]Y. Murai, Y. Tasaka, T. Nambu, Y. Takeda, and S. R. Gonzalez, "Ultrasonic detection of moving interfaces in gas-liquid two-phase flow," Flow Meas. Instrum. **21**, 356–366 (2010).

[48]D. Yoon, H. J. Park, and T. Ihara, "Development of an instantaneous velocity-vector-profile method using conventional ultrasonic transducers," Meas. Sci. Technol. **33**, 035301 (2021).

[49]H. Murakawa, K. Sugimoto, and N. Takenaka, "Effects of the number of pulse repetitions and noise on the velocity data from the ultrasonic pulsed Doppler method with different algorithms," Flow Meas. Instrum. **40**, 9–18 (2014).

[50]C. Kasai, K. Namekawa, A. Koyano, and R. Omoto, "Real-time two-dimensional blood flow imaging using an autocorrelation technique," IEEE Trans. Sonics Ultrason. **32**, 458–464 (1985).